






Ground state magnetic structure and magnetic field effects in the layered honeycomb antiferromagnet YbOCl

Zheng Zhang ¹, Yanzhen Cai ², Jinlong Jiao,³ Jing Kang,¹ Dehong Yu ⁴, Bertrand Roessli,⁵ Anmin Zhang,² Jianting Ji ¹,
Feng Jin,¹ Jie Ma ^{3,*} and Qingming Zhang^{1,2,†}

¹Beijing National Laboratory for Condensed Matter Physics, Institute of Physics, Chinese Academy of Sciences, Beijing 100190, China

²School of Physical Science and Technology, Lanzhou University, Lanzhou 730000, China

³Department of Physics and Astronomy, Shanghai Jiao Tong University, Shanghai 200240, China

⁴Australian Nuclear Science and Technology Organisation, Lucas Heights, New South Wales 2232, Australia

⁵Laboratory for Neutron Scattering and Imaging, Paul Scherrer Institut, 5232 Villigen, Switzerland



(Received 16 July 2023; revised 30 May 2024; accepted 28 August 2024; published 10 September 2024)

YbOCl is a representative member of the van der Waals layered honeycomb rare-earth chalcogenide $R\text{ChX}$ (R = rare earth; Ch = O, S, Se, and Te; and X = F, Cl, Br, and I) family reported recently. Its spin ground state remains to be explored experimentally. We grew high-quality single crystals of YbOCl and conducted comprehensive thermodynamic, elastic, and inelastic neutron scattering experiments down to 50 mK. The experiments reveal an antiferromagnetic phase below 1.3 K which is identified as a spin ground state with an intralayer ferromagnetic and interlayer antiferromagnetic ordering. By applying sophisticated numerical techniques to a honeycomb (nearest-neighbor)–triangle (next-nearest-neighbor) model Hamiltonian which accurately describes the highly anisotropic spin system, we are able to simulate the experiments well and determine the diagonal and off-diagonal spin-exchange interactions. The simulations give an antiferromagnetic Kitaev term comparable to the Heisenberg one. The experiments under magnetic fields allow us to establish a magnetic field–temperature phase diagram around the spin ground state. Most interestingly, a relatively small magnetic field (~ 0.3 to 3 T) can significantly suppress the antiferromagnetic order, suggesting an intriguing interplay of the Kitaev interaction and magnetic fields in the spin system. The present study provides fundamental insights into the highly anisotropic spin systems and opens a window to look into Kitaev spin physics in a rare-earth-based system.

DOI: [10.1103/PhysRevResearch.6.033274](https://doi.org/10.1103/PhysRevResearch.6.033274)

I. INTRODUCTION

Among the various proposed quantum spin liquid models, the exactly solvable Kitaev spin liquid (KSL) model built on a honeycomb lattice has garnered significant interest due to its fundamental importance and potential applications in topological quantum computing. However, the material realization of KSL remains a crucial challenge, owing to the rather unusual bond-dependent spin interactions. In recent years, the efforts in searching for the KSL candidates have been focused on $4d/5d$ ions, such as iridate $A_2\text{IrO}_3$ (A = Li, Na, and Cu) [1–6] and $\alpha\text{-RuCl}_3$ [7–10]. In general, rare-earth magnetic ions exhibit highly anisotropic magnetism stemming from the strong spin-orbit coupling (SOC) and can naturally serve as building blocks for Kitaev materials through the Jackeli-Khaliullin mechanism [11]. Particularly, rare-earth ions with an odd number of $4f$ electrons possess a doubly degenerate crystalline electric field (CEF) ground state (Kramers

doublets), which is protected by time-reversal symmetry and yields the effective spin-1/2 required by KSL. Due to the critical experimental requirements, Kitaev spin systems based on rare-earth magnetic ions remain less explored [12,13].

Recently, we revealed a family of KSL candidates, namely, rare-earth chalcogenides $R\text{ChX}$ (R = rare-earth; Ch = O, S, Se, and Te; X = F, Cl, Br, and I) [14,15]. Most of the family members possess a high symmetry of $R\text{-}3m$, with nearest rare-earth magnetic ions forming an undistorted honeycomb lattice. Furthermore, the van der Waals layered rare-earth chalcogenides offer good two-dimensionality, which is crucial for Abelian and non-Abelian excitations in KSLs and conducive to the fundamental study and potential applications based on atomically thin flakes.

Following the initial discovery, we have successfully grown sizable single crystals of YbOCl (~ 15 mm maximum), providing an exceptional opportunity for in-depth experimental studies on the spin systems. In our previous work, we conducted thermodynamic measurements above 1.8 K, examined CEF excitations, and initially studied the theoretical ground state phase diagram [15]. Experimental investigation of the spin ground state, which is a fundamental issue in the search for the KSL phase, remains unexplored so far in this spin system.

In this paper, we concentrate on the experimental exploration of the spin ground state in YbOCl. The magnetization

*Contact author: jma3@sjtu.edu.cn

†Contact author: qmzhang@iphy.ac.cn

Published by the American Physical Society under the terms of the Creative Commons Attribution 4.0 International license. Further distribution of this work must maintain attribution to the author(s) and the published article's title, journal citation, and DOI.

and heat capacity measurements indicate that YbOCl undergoes an antiferromagnetic (AFM) transition at 1.3 K. Elastic neutron scattering experiments down to 50 mK have shown magnetic Bragg peaks below 1.3 K and have determined the magnetic propagation vector \vec{Q} to be $[0, 0, 1.5]$. A honeycomb-triangle spin Hamiltonian including the nearest-neighbor (NN) and next-nearest-neighbor (NNN) spin interactions is proposed to accurately describe the spin system. The full diagonalization (FD) simulations for magnetization and heat capacity under high magnetic fields determine the spin interactions in the Hamiltonian. The spin interactions are jointly determined by simulating the inelastic neutron scattering (INS) spectra of polycrystalline samples in the ordered phase with linear spin wave theory. The obtained Kitaev interaction is comparable to the Heisenberg one. Using the spin parameters, density matrix renormalization group (DMRG) calculations give an A-type AFM phase, i.e., an AFM ordering along the c axis accompanied by in-plane ferromagnetic ordering, quantitatively in agreement with neutron and thermodynamic measurements. The neutron scattering and thermodynamic measurements under magnetic fields allow us to establish a magnetic field–temperature phase (H - T) diagram around the ground state. Interestingly, the AFM order is suppressed by a modest magnetic field of ~ 0.3 T in YbOCl, indicating that the zero-field AFM ground state exhibits notable Kitaev interactions. The application of external magnetic fields, serving as a transverse field term, accentuates quantum fluctuations, suggesting an intricate connection between these fluctuations and the proximity to the Kitaev spin-liquid-like behavior.

II. SAMPLES, EXPERIMENTS, AND METHODS

YbOCl crystals were grown using the anhydrous YbCl₃-flux method [14]. X-ray diffraction and energy dispersive x-ray measurements confirmed the high quality of the samples [15]. Nearly 5 mg of YbOCl single crystals were prepared for thermodynamics measurements. The principal axes of the single crystals were determined using Laue diffraction in combination with an optical microscope for further measurements. The temperature dependent magnetization (M / H - T) and magnetic field dependent magnetization (M - H) measurements along the c axis and a axis from 0.5 to 2 K under magnetic field were carried out using a Quantum Design magnetic property measurement system with a ³He refrigerator. M / H - T and M - H measurements along the c axis and a axis from 1.8 to 100 K under magnetic field were carried out using a Quantum Design physical property measurement system (PPMS) with a vibrating sample magnetometer. Heat capacity and AC susceptibility from 50 mK to 4 K under magnetic field were measured using a Quantum Design PPMS with a dilution refrigerator. Elastic neutron scattering was conducted on ~ 2 g polycrystalline samples down to 50 mK, and the reflections were determined using FULLPROF [16] software. The magnetic symmetry approach is available on the Bilbao Crystallographic Server [17]. Approximately 150 single-crystal pieces, totaling around 0.2 g of YbOCl, were meticulously coaligned in the (HOL) scattering plane on copper plates for the neutron experiment to detect the magnetic Bragg peaks. This experiment was conducted using the cold-neutron Triple-Axis Spectrometer (TASP) at the Swiss Neutron Spal-

ation Source (SINQ), located at the Paul Scherrer Institut in Switzerland. The measurements on TASP were completed with a fixed $E_f = 3.5$ meV. A horizontal field cryomagnet, specifically MA02, equipped with a dilution refrigerator was used to generate a maximum magnetic field of 2 T at temperatures as low as 0.12 K. This setup enabled the application of magnetic fields along the c axis during the experiment. The 12-spin-site FD was employed to simulate M / H - T , M - H , and heat capacity data under different magnetic fields. The ground state magnetic structure on a quasi-two-dimensional plane composed of magnetic ions was calculated using the DMRG method [18,19]. The periodic boundary conditions (PBC) was employed to get accurate DMRG results. The clusters used in the DMRG simulations are $L_x \times L_y = 12 \times 6$ and $L_x \times L_y = 12 \times 12$. The truncation error was kept below 10^{-5} , and we performed 30 sweeps to improve the accuracy of the simulations. The powder-averaged spin wave calculations along a specified path in the Brillouin zone were based on the SPINW package [20].

III. MODEL HAMILTONIAN

YbOCl has a structure of two adjacent triangular magnetic layers. The distance between the NNN magnetic ions (~ 3.73 Å) is comparable to that between the NN magnetic ions (~ 3.55 Å). We can get a more accurate description of the spin system by taking the NNN spin interactions into account [Fig. 1(a)]. The honeycomb spin lattice formed by the NN magnetic ions [Fig. 1(b)] strictly satisfies the threefold rotational symmetry C_3 required by the Kitaev model, while the triangular lattice formed by the NNN magnetic ions [Fig. 1(c)] follows the sixfold rotational symmetry C_6 . Considering the strong SOC of Yb³⁺ and the local octahedral structure, the off-diagonal spin interactions are expected to play an important role. Therefore, the NN spin Hamiltonian can be represented as follows [21]:

$$\begin{aligned} \hat{H}_{\text{Honeycomb}} = & \sum_{\langle ij \rangle} J_{zz} S_i^z S_j^z + J_{\pm} (S_i^+ S_j^- + S_i^- S_j^+) \\ & + J_{\pm\pm} (\gamma_{ij} S_i^+ S_j^+ + \gamma_{ij}^* S_i^- S_j^-) \\ & + J_{z\pm} (\gamma_{ij} S_i^+ S_j^z + \gamma_{ij}^* S_i^- S_j^z + \langle i \leftrightarrow j \rangle), \quad (1) \end{aligned}$$

where J_{zz} , J_{\pm} , $J_{\pm\pm}$, and $J_{z\pm}$ are the NN spin-exchange interactions, γ_{ij} corresponds to 1, $e^{2i\pi/3}$, and $e^{-2i\pi/3}$ along the three bonds of δ_1 , δ_2 , and δ_3 in the honeycomb lattice [Fig. 1(b)]. The NNN spin Hamiltonian follows [22]:

$$\begin{aligned} \hat{H}_{\text{Triangular}} = & \sum_{\langle\langle ik \rangle\rangle} J'_{zz} S_i^z S_k^z + J'_{\pm} (S_i^+ S_k^- + S_i^- S_k^+) \\ & + J'_{\pm\pm} (\gamma'_{ik} S_i^+ S_k^+ + \gamma'_{ik}{}^* S_i^- S_k^-) \\ & - \frac{iJ'_{z\pm}}{2} (\gamma'_{ik}{}^* S_i^+ S_k^z + \gamma'_{ik} S_i^- S_k^z + \langle i \leftrightarrow k \rangle), \quad (2) \end{aligned}$$

where J'_{zz} , J'_{\pm} , $J'_{\pm\pm}$, and $J'_{z\pm}$ are the NNN spin-exchange interactions and γ'_{ik} corresponds to 1, $e^{2i\pi/3}$, and $e^{-2i\pi/3}$ along the other three bonds, δ'_1 , δ'_2 , and δ'_3 , in the triangular lattice [Fig. 1(c)]. As a higher-order term, Dzyaloshinskii-Moriya interaction is neglected here. The model Hamiltonian sets a foundation on which we can carry out quantitative

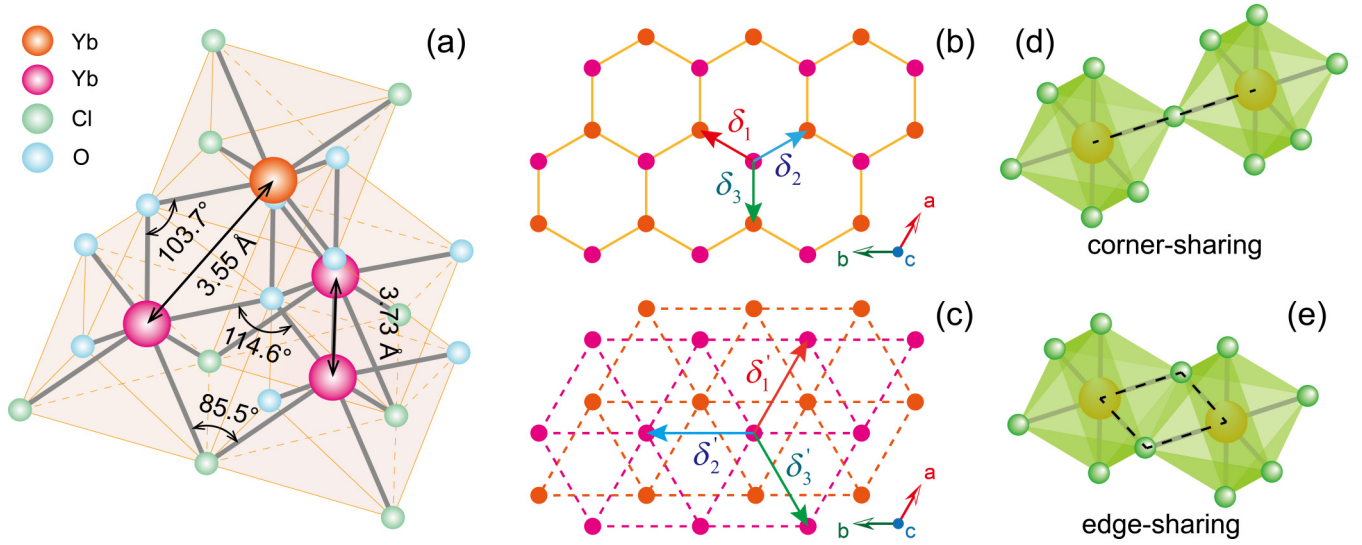


FIG. 1. Local environment around Yb^{3+} in YbOCl . (a) The octahedral structure formed by Yb^{3+} ions and surrounding anions, as well as the bond lengths and bond angles between nearest-neighbor (NN) magnetic ions and next-nearest-neighbor (NNN) magnetic ions. (b) A honeycomb lattice structure formed by NN magnetic ions. (c) A double-layer triangular lattice structure formed by NNN magnetic ions. (d) The schematic of a corner-sharing structure. (e) The schematic of an edge-sharing structure.

analysis and simulations of the thermodynamic and neutron experiments.

Further analysis of the spin Hamiltonian for YbOCl can be conducted. First, the spin Hamiltonian is equivalent to the J - K - Γ - Γ' model [21,23,24], which allows mutual conversion of spin-exchange parameters between the two models. The transformation formulas between the spin Hamiltonian and J - K - Γ - Γ' in the honeycomb lattice are as follows [21]:

$$\begin{aligned}
 J_1 &= \frac{4}{3}J_{\pm} - \frac{2\sqrt{2}}{3}J_{z\pm} - \frac{2}{3}J_{\pm\pm} + \frac{1}{3}J_{zz}, \\
 K_1 &= 2\sqrt{2}J_{z\pm} + 2J_{\pm\pm}, \\
 \Gamma_1 &= -\frac{2}{3}J_{\pm} - \frac{2\sqrt{2}}{3}J_{z\pm} + \frac{4}{3}J_{\pm\pm} + \frac{1}{3}J_{zz}, \\
 \Gamma'_1 &= -\frac{2}{3}J_{\pm} + \frac{2\sqrt{2}}{3}J_{z\pm} - \frac{4}{3}J_{\pm\pm} + \frac{1}{3}J_{zz}. \quad (3)
 \end{aligned}$$

Similarly, the transformation formulas between the spin Hamiltonian and J - K - Γ - Γ' in the triangular lattice are as follows [23]:

$$\begin{aligned}
 J_2 &= \frac{1}{3}(2J'_{\pm\pm} + J'_{zz} + 2J'_{\pm\pm} + \sqrt{2}J'_{z\pm}), \\
 K_2 &= -2J'_{\pm\pm} - \sqrt{2}J'_{z\pm}, \\
 \Gamma_2 &= \frac{1}{3}(-J'_{\pm} + J'_{zz} - 4J'_{\pm\pm} + \sqrt{2}J'_{z\pm}), \\
 \Gamma'_2 &= \frac{1}{6}(-2J'_{\pm} + 2J'_{zz} + 4J'_{\pm\pm} - \sqrt{2}J'_{z\pm}). \quad (4)
 \end{aligned}$$

From the transformation formulas, it is evident that the Kitaev terms are associated with off-diagonal interactions in both the honeycomb and triangular lattices. In rare-earth magnetic ions, the strong SOC generates significant magnetic anisotropy, which lays the foundation for exploring Kitaev physics in rare-earth magnets. Second, we can discuss the origins of Kitaev interactions from a crystallographic perspective [25]. Two types of configurations involving magnetic ions are

frequently observed in various magnetic materials: one is the corner-sharing configuration shown in Fig. 1(d), and the other is the edge-sharing configuration depicted in Fig. 1(f). For the corner-sharing configuration, the bond angle formed by the magnetic ion, the coordinating anion, and another magnetic ion is 180° , the Kitaev interaction K can be completely canceled out. For the edge-sharing configuration, the bond angle formed by the magnetic ion, the coordinating anion, and another magnetic ion is 90° ; the Heisenberg interaction J can be completely canceled. If the magnetic ions and coordinating ions can form a perfect cubic structure, the off-diagonal terms Γ and Γ' in the J - K - Γ - Γ' model vanish completely. In real materials, achieving the ideal crystal structure mentioned above is challenging; hence, terms like J , K , Γ , and Γ' are present. Considering these factors, the application of the spin Hamiltonians described by Eqs. (1) and (2) is reasonable for YbOCl .

IV. MAGNETIC PHASE TRANSITION OF YbOCl

The M/H - T measurements along the c axis and a axis [Fig. 2(a)] under 0.01 T reveal a transition at 1.3 K. The absence of hysteresis loops in the M - H curve at 0.5 K suggests that it is an AFM transition [24]. A small magnetic field of ~ 0.1 T saturates the magnetic moments along the a axis, while the saturation along the c axis occurs at around 3.5 T [Fig. 2(b)]. The strong anisotropy is consistent with an in-plane ferromagnetic ordering and an AFM ordering along the c axis, which will be clarified later with more neutron experiments and simulations. The transition is also evidenced by heat capacity measurements from 50 mK to 4 K [see Fig. 4(a) below]. The magnetic entropy has not fully reverted to $R \ln 2$ up to 4 K [24], and a higher temperature is required to completely achieve spin disordering. This means that an effective spin-1/2 model remains valid for the spin system below 4 K.

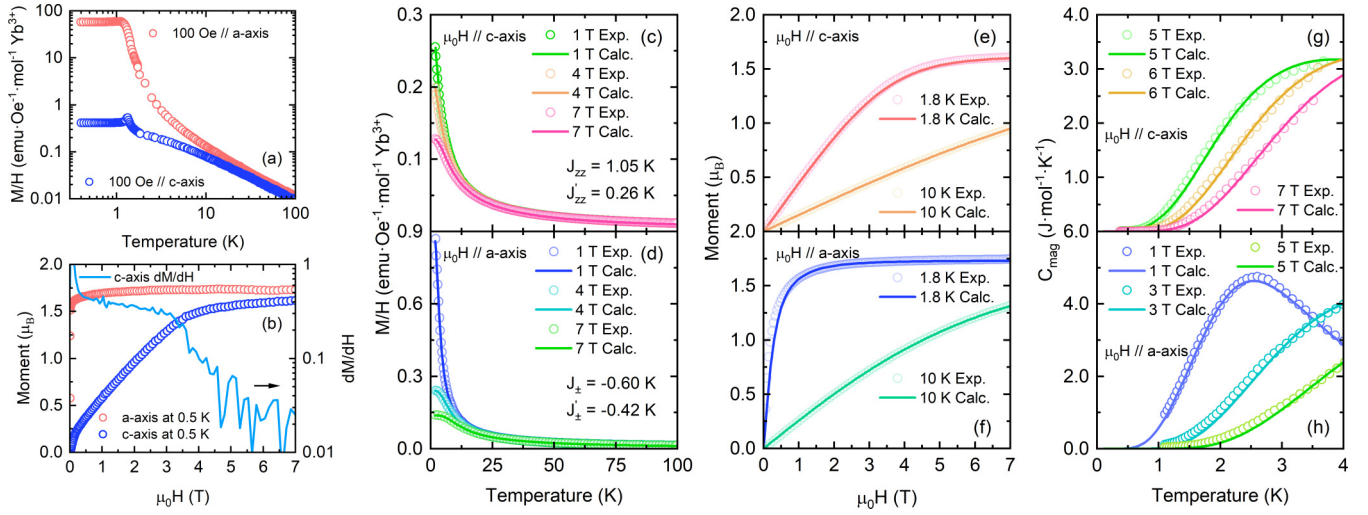


FIG. 2. Magnetization and heat capacity under magnetic fields. (a) and (b) M/H - T and M - H along the a axis (red circles) and along the c axis (blue circles) in YbOCl at low temperatures. M/H - T data (open circles) and the simulations (solid lines) along (c) the c axis and (d) the a axis under different magnetic fields. (e) The M - H data along the c axis (open circles) and the simulations (solid lines) and (f) those along the a axis at 1.8 and 10 K. Magnetic heat capacity under magnetic fields along (g) the c axis and (h) the a axis. The open circles and the solid lines represent the experiments and the simulations, respectively.

The exchange parameters in the spin Hamiltonian are jointly determined by simulating thermodynamic data under high magnetic fields with FD calculations and INS spectra with linear spin wave theory.

The diagonal spin interactions J_{zz} , J'_{zz} , J_{\pm} , and J'_{\pm} are first given by the fitting of M/H - T data. In the paramagnetic state and under high magnetic fields, spins are fully polarized, and the off-diagonal terms can be ignored. The high-temperature series expansion technique confirms that the effect of the diagonal terms on susceptibility decays as T^{-2} with temperature, while for the off-diagonal ones it decays as T^{-3} in a specified direction [21,22]. This is also verified by our numerical calculations, which show little difference in simulating M/H - T curves with and without the off-diagonal interactions in the low-temperature (~ 1.8 K) range [24].

The M/H - T measurements under magnetic field along the c axis and a axis from 1.8 to 100 K are shown in Figs. 2(c) and 2(d), respectively. The 12-spin-site FD simulations of the M/H - T data output an optimal set of parameters, namely, $J_{zz} = 1.05$ K, $J'_{zz} = 0.26$ K, $J_{\pm} = -0.6$ K, and $J'_{\pm} = -0.42$ K. The parameters allow us to reproduce M/H - T under other magnetic fields [24] and M - H curves at 1.8 and 10 K [Figs. 2(e) and 2(f)], which are highly consistent with the experimental results. The square norm of the residuals is 9.306×10^{-4} for J_{zz} and J'_{zz} and 0.011 for J_{\pm} and J'_{\pm} .

Heat capacity generally reflects the energy spectrum of microscopic states. The off-diagonal terms are automatically included in the magnetic heat capacity. Therefore, the off-diagonal terms can be obtained by simulating magnetic heat capacity under high magnetic fields.

The magnetic moments along the c axis and a axis at 1.8 K saturate at 5 and 1 T, respectively. Therefore, magnetic heat capacity measurements under 5, 6, and 7 T along the c axis and 1, 3, and 5 T along the a axis are carried out [Figs. 2(g) and 2(h)]. The FD simulations give off-diagonal terms of $J_{\pm\pm} = 0.39$ K, $J'_{\pm\pm} = 0.13$ K, $J_{z\pm} \sim 0$, and $J'_{z\pm} \sim 0$. We sum-

marize these fitted parameters in Table I. The square norms of the residuals of $J_{\pm\pm}$, $J'_{\pm\pm}$, $J_{z\pm}$, and $J'_{z\pm}$ are 0.77. The DMRG calculations verify that both $J_{z\pm}$ and $J'_{z\pm}$ are close to zero [24].

Meanwhile, the INS spectrum down to 50 mK was measured [Fig. 3(d)] and employed to make a joint determination of the exchange parameters. The exchange parameters given by thermodynamic experiments are applied to the spin Hamiltonian to simulate the powder-averaged INS spectrum at 50 mK with linear spin wave (LSW) theory. The optimized LSW calculations accurately reproduce the experimental magnetic excitations [Fig. 3(e)]. The exchange parameters examined and refined by the LSW simulations are finally pinned down. We also calculated the dispersion of YbOCl along the specified paths [Fig. 3(f)] in the Brillouin zone, as shown in Fig. 3(g). The calculations reveal no dispersion from the G point to the A point, aligning with the perfect two-dimensional properties of YbOCl, which suggest a lack of interlayer spin-exchange interactions. Excitations from the M point through the G point to the K point manifest a distinct V-shaped structure, aligning closely with features observed at low $|\vec{Q}|$ in the powder INS spectrum. This offers a valuable reference for future investigations of the INS spectra of YbOCl single crystals.

Based on Eqs. (3) and (4), we can transform spin-exchange parameters between the two models, resulting in $J_1 \sim -0.71$ K, $K_1 \sim 0.78$ K, $\Gamma_1 \sim 1.27$ K, and $\Gamma'_1 \sim 0.49$ K for the honeycomb lattice and $J_2 \sim -0.11$ K, $K_2 \sim -0.26$ K, $\Gamma_2 \sim 0.05$ K, and $\Gamma'_2 \sim 0.07$ K for the triangular lattice. To compare these parameters more clearly, we summarize them in Table II.

For the J - K - Γ - Γ' model, it is clearer that the NNN spin interactions are significantly smaller than the NN ones, demonstrating that the spin interactions in the honeycomb lattice play a major role in the magnetism of YbOCl. Although the ferromagnetic Heisenberg interactions lead to a magnetically ordered ground state in YbOCl, the

TABLE I. Spin-exchange interactions in the model Hamiltonian.

J_{zz} (K)	J_{\pm} (K)	$J_{\pm\pm}$ (K)	$J_{z\pm}$ (K)	J'_{zz} (K)	J'_{\pm} (K)	$J'_{\pm\pm}$ (K)	$J'_{z\pm}$ (K)
1.05	-0.6	0.39	0	0.26	-0.42	0.13	0

antiferromagnetic Kitaev interaction ($K_1 > 0$) in YbOCl provides the possibility to explore richer Kitaev physics [26,27]. The positive Kitaev term, compared to the negative one in α -RuCl₃ [28], is more likely to host stable topological excitations. The ratio $|K_1/J_1| \sim 1.1$, comparable to those in α -RuCl₃ [28,29] and Na₂Co₂TeO₆ [30], indicates that Kitaev spin physics plays an essential role in YbOCl. The relatively large off-diagonal terms Γ_1 and Γ'_1 are directly related to the octahedral structure of YbCl₃O₄ with distortions.

V. GROUND STATE MAGNETIC STRUCTURE

We conducted elastic neutron scattering experiments on polycrystals down to 50 mK to determine the ground state magnetic structure of YbOCl. Three new reflections at $|\vec{Q}| = 0.33 \text{ \AA}^{-1}$, $|\vec{Q}| = 1.70 \text{ \AA}^{-1}$, and $|\vec{Q}| = 2.03 \text{ \AA}^{-1}$ in the spin-ordered phase are highlighted using the spectrum at 8 K as the background [Fig. 3(b)]. The analysis and fitting based on the FULLPROF program [16] determine that the wave vectors of the magnetic Bragg reflections are $[0, 0, 1.5]$, $[0, 0, 7.5]$, and

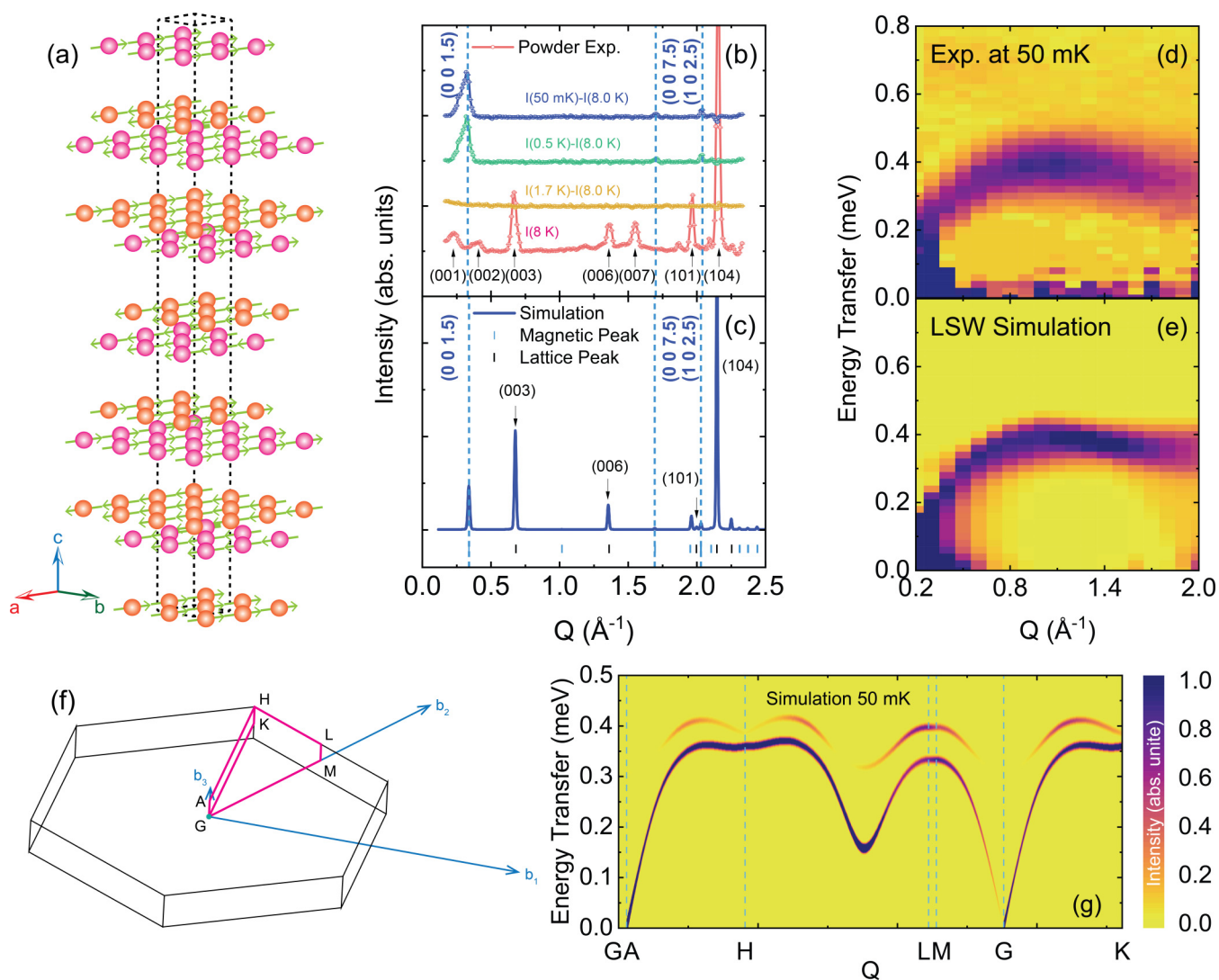


FIG. 3. Ground state magnetic structure and neutron scattering experiments. (a) The three-dimensional ground state magnetic structure of YbOCl with the magnetic propagation vector $\vec{Q} = [0, 0, 1.5]$. (b) The elastic neutron scattering spectra on polycrystals down to 50 mK. The blue dashed lines mark the magnetic Bragg peaks below the transition temperature 1.3 K. (c) Elastic neutron scattering spectrum simulated with the magnetic structure of YbOCl. The black numbers mark the wave vectors of the magnetic peaks, and the blue numbers mark the lattice vectors. (d) The experimental INS spectrum on polycrystals at 50 mK. (e) The simulated powder-averaged INS by linear spin wave theory. (f) The Brillouin zone of YbOCl. The red solid lines mark the path connecting the high-symmetry points in the Brillouin zone. (g) The simulated INS spectrum of YbOCl based on the LSW theory.

TABLE II. Spin-exchange interactions in the J - K - Γ - Γ' model.

J_1 (K)	K_1 (K)	Γ_1 (K)	Γ'_1 (K)	J_2 (K)	K_2 (K)	Γ_2 (K)	Γ'_2 (K)
-0.71	0.78	1.27	0.49	-0.11	-0.26	0.05	0.07

[1, 0, 2.5], respectively, and the magnetic propagation vector is determined to be $\vec{Q} = [0, 0, 1.5]$. Hence, a ferromagnetic magnetic structure forms within the ab plane, while an AFM structure develops along the c axis. The three-dimensional ground state magnetic structure is shown in Fig. 3(a). Combining the magnetization data from Figs. 2(a) and 2(b), we can infer that the in-plane ferromagnetic structure in YbOCl primarily arises from anisotropic spin-exchange interactions, whereas the antiferromagnetic alignment along the c axis is associated with the interlayer van der Waals forces. Since our focus is on quantum magnetism resulting from spin-exchange interactions, it is reasonable to overlook the interlayer van der Waals forces in the analysis of the magnetism of YbOCl.

The magnetic structure is also supported by INS experiments at 50 mK [Fig. 3(d)], as mentioned above. Additionally, it is further examined by two-dimensional DMRG calculations with the experimentally determined exchange parameters, which demonstrate that the magnetic moments almost lie in the ab plane and form a ferromagnetic ordering along the a axis [24].

The in-plane ferromagnetic and interlayer AFM ordering in YbOCl is distinct from the observations in some other Kitaev compounds. For instance, the ground state magnetic structure in α -RuCl₃ [31] and Na₂IrO₃ [2,32] is a zigzag-ordered state, and the ground state of YbCl₃ [12,13,33] is a Néel one. The difference is closely related to the fact that J_{\pm} and J'_{\pm} are negative (ferromagnetic), while J_{zz} and J'_{zz} are positive (AFM) in YbOCl.

VI. FIELD EFFECTS AND H - T PHASE DIAGRAM

We investigated the ground state magnetism of YbOCl under magnetic field along the c axis (Fig. 4). The transition is gradually suppressed by increasing the magnetic field [Figs. 4(a) and 4(b)]. Elastic neutron scattering provides clear evolution of the magnetic Bragg peak at $\vec{Q} = [0, 0, -1.5]$ with a magnetic field [Figs. 4(d) and 4(e)]. The magnetic Bragg peak decreases with increasing field and becomes almost invisible for a field ≥ 0.3 T. Hence, a relatively small magnetic field can suppress the magnetic phase transition. This coincides with the plateau observed in the χ' - H [Fig. 4(c)] and dM/dH - H [Fig. 2(b)] curves in the range of 0.3 to 3.1 T.

Interestingly, the transition shifts to higher temperatures with increasing magnetic field. This has been consistently seen in the heat capacity, M/H - T , and AC susceptibility [24], distinct from a conventional AFM transition, which usually shifts to lower temperature with magnetic field. The unusual magnetic field dependence in YbOCl arises from the highly anisotropic spin interactions caused by the strong SOC in Yb³⁺ ions. For comparison, α -RuCl₃ [34–36], YbCl₃ [13,33], and Na₂Co₂TeO₆ [37] demonstrate the evolution of a conventional AFM with magnetic field.

The above experiments and analysis allow us to establish the H - T phase diagram [Fig. 4(f)]. The H - T phase diagram

can be divided into five regions. First of all, the red dashed line marks the paramagnetic state, distinct from other spin phases, at higher temperatures. Below ~ 1.3 K, the spin system undergoes four states with increasing magnetic field, i.e., a spin-ordered state, a transition state, a possible spin-disordered phase, and a spin-polarized state. We provide more detailed discussion in the following.

The small dip around 0.02 T in the AC susceptibility χ' marks the boundary from the spin-ordered state to a transition state. It stems from the weak interlayer AFM coupling, which can be easily disrupted by an external magnetic field. The transition state covers the range of 0.02 to 0.3 T. In addition to the aforementioned thermodynamic data, single-crystal elastic neutron scattering experiments under a magnetic field along the c axis also demonstrate that the magnetic Bragg reflection of $[0, 0, -1.5]$ is gradually suppressed with magnetic field, suggesting a transition state or crossover before entering the spin-disordered state. At higher magnetic fields above ~ 3.1 T, the system enters a fully polarized state, with a rapid drop in both AC susceptibility χ [Fig. 4(c)] and dM/dH - H [Fig. 2(b)].

The possible spin-disordered phase in the range of 0.3 to 3.1 T is of particular interest. In this region, the transition peaks in heat capacity and M/H - T fade away with magnetic field, and a clear plateau appears in the AC susceptibility [Fig. 4(c)]. Generally, AC magnetic susceptibility can be regarded as a spin response function and acts as a good indicator of spin fluctuations in a spin system [38]. The formula for the definition of AC magnetic susceptibility is as follows:

$$\chi' = \lim_{\mu_0 H \rightarrow 0} \frac{\partial \langle M \rangle}{\partial \mu_0 H} = \frac{\langle M^2 \rangle - \langle M \rangle^2}{k_B T}. \quad (5)$$

The plateaulike feature in the AC susceptibility χ' corresponds to a region in which spin fluctuations are enhanced by magnetic fields. The feature is verified by the derivatives of M - H curves [Fig. 2(b)]. More crucially, the nearly complete suppression of the magnetic Bragg peak at $\vec{Q} = [0, 0, -1.5]$ by a magnetic field above 0.3 T clearly indicates that the AFM order is suppressed by magnetic fields. The region of enhanced spin fluctuations may potentially represent a KSL-like state. If the spins were merely aligned along the c axis with increasing magnetic fields, the AC susceptibility χ' would not exhibit a sustained robust plateau between 0.3 and 3.1 T. On the other hand, we consider it unlikely that the magnetic moments gradually polarize along the c -axis direction within the magnetic field range of 0.3 to 3 T. If we follow this perspective, the magnetic Bragg peak at $\vec{Q} = [0, 0, 1.5]$ should not completely disappear before the spins are fully polarized. Conversely, elastic neutron scattering data demonstrate that the magnetic Bragg peak at $\vec{Q} = [0, 0, 1.5]$ vanishes at fields exceeding 0.3 T, which is markedly different from the saturation field of 4 T. We also estimate the Zeeman energy scale using the experimentally determined parameters. The Zeeman term is $\mu_0 \mu_B g_c H_c$ (μ_B is the Bohr magneton, $g_c \sim 3.2$ is

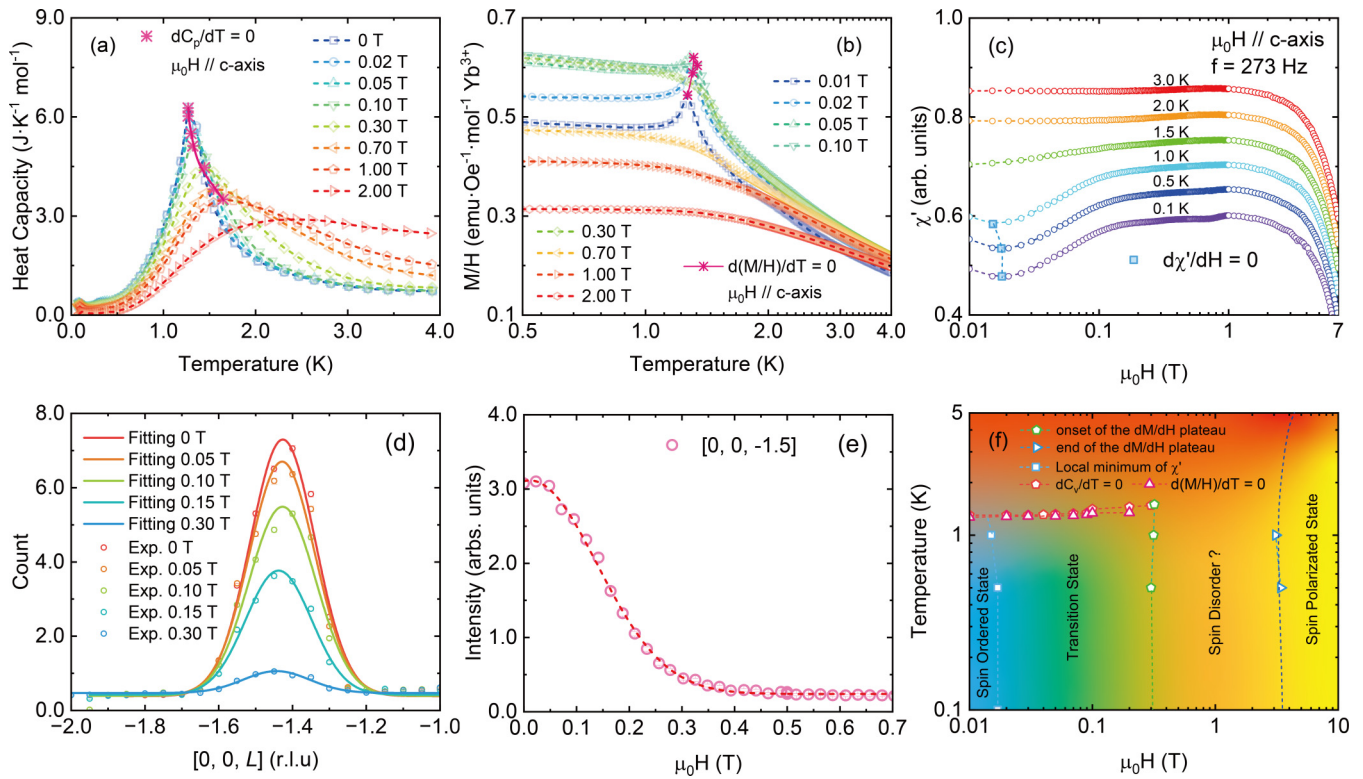


FIG. 4. Magnetic field dependent experiments and H - T phase diagram. (a) Heat capacity under magnetic fields along the c axis. The red stars trace the peak change in heat capacity with magnetic fields. (b) M/H - T under magnetic fields along the c axis. The red stars mark the evolution of the phase transition with magnetic fields. More heat capacity and M/H - T data can be found in the Supplemental Material [24]. (c) AC susceptibility χ' along the c axis at different temperatures. The blue squares mark the local minimum of χ' . (d) The single-crystal neutron diffraction scans in the momentum range of \bar{Q} from $[0, 0, -2]$ to $[0, 0, -1]$ with magnetic fields at 0.13 K. The circles represent the experimental results, and the solid lines are the fitting ones. (e) The scattering intensity of the magnetic Bragg reflection $\bar{Q} = [0, 0, -1.5]$ varies with magnetic field at 0.13 K. (f) The H - T phase diagram is determined by heat capacity, M/H - T , and AC susceptibility χ' along the c axis. The phase boundaries are marked by the red pentagons and red upward triangles with the criteria $dC_p/dT = 0$ and $d(M/H)/dT = 0$, respectively. The blue squares indicate the boundaries between the spin-ordered phase and the transition state by the local minimum of the AC susceptibility χ' . The green pentagons and blue inverted triangles respectively denote the boundaries between the possible spin-disordered phase and the transition state and between the possible spin-disordered phase and the spin-polarized state.

Landé g factor along the c axis, and H_c is the magnetic field), and a magnetic field of 0.3 T is about 0.6 K. For comparison, the spin interaction is approximately 1.0 K. The energy scale contributed by the magnetic field is insufficient to drive the spins into a polarized state.

The unusual behavior seems to be related to the fact that the magnetic moment in the ab plane is significantly larger than that along the c axis. Therefore, the magnetic field acts as an effective transverse field along the c axis, which essentially enhances quantum fluctuations and suppresses the magnetically ordered state, along with the off-diagonal spin interactions. A similar magnetic field dependent behavior has been witnessed in other KSL candidates, such as α - RuCl_3 [7,8,39,40] and $\text{Na}_2\text{Co}_2\text{TeO}_6$ [37,41–43]. All of them show a spin-ordered ground state at 0 T and are tuned into a KSL-like state by applying magnetic field. It should be noted that the critical magnetic field is ~ 7 T for α - RuCl_3 , ~ 7.5 T for $\text{Na}_2\text{Co}_2\text{TeO}_6$, and only ~ 0.3 T for YbOCl . The greatly reduced critical field in YbOCl stems from the strong screening of $4f$ electrons by the outer $5s$ and $5p$ shells. This offers the significant advantage of easy manipulation of a potential KSL phase, making YbOCl a unique and promising

candidate for further exploration in this intriguing area of research.

The emergence of the KSL-like state in YbOCl is accompanied by several quantum phase transitions and quantum critical points, i.e., from the spin-ordered state to the KSL-like state and from the KSL-like state to the fully polarized state. The unusual KSL-like phase itself and the quantum phase transitions are expected to offer rich Kitaev spin physics, which will require extensive deep theoretical and experimental exploration in the future.

VII. SUMMARY

In this study, we experimentally explored the magnetic ground state in the newly reported layered honeycomb antiferromagnet YbOCl and discovered a possible spin liquid phase. By combining thermodynamic and neutron measurements with sophisticated numerical simulations, the fundamental diagonal and off-diagonal exchange coupling parameters for the highly anisotropic spin system were determined, which quantitatively pinned down the spin Hamiltonian. The compound undergoes an AFM transition at 1.3 K. The neutron scattering

experiments down to 50 mK and DMRG calculations and spin wave calculations consistently point to a magnetic ground state with a magnetic propagation vector $\vec{Q} = [0, 0, 1.5]$. The experiments allowed us to establish an H - T phase diagram. Most interestingly, the ordered ground state can be pushed into a spin-disordered state with enhanced quantum spin fluctuations (or a possible KSL phase) using a small magnetic field (~ 0.3 T). The present study demonstrates that the van der Waals layered family offers an inspiring playground for anisotropic spin systems, particularly for Kitaev spin physics and potential applications.

ACKNOWLEDGMENTS

This work was supported by the National Key Research and Development Program of China (Grant No.

2022YFA1402700), the National Science Foundation of China (Grant No. 12274186), the Strategic Priority Research Program of the Chinese Academy of Sciences (Grant No. XDB33010100), and the Synergetic Extreme Condition User Facility (SECUF). A portion of this work was performed on the Steady High Magnetic Field Facility, High Magnetic Field Laboratory, CAS. The neutron scattering data were collected at the Bragg Institute of the Australian Nuclear Science and Technology Organisation (ANSTO) using the PELICAN time-of-flight spectrometer. We all acknowledge the beam time granted by ANSTO (Proposal No. P7489). The neutron scattering data on single crystals were collected on the cold-neutron Triple-Axis Spectrometer (TASP) at the Swiss Neutron Spallation Source SINQ, Paul Scherrer Institut (PSI), Switzerland. We all acknowledge the beam time granted by PSI (Proposal No. 20221067).

-
- [1] T. Takayama, A. Kato, R. Dinnebier, J. Nuss, H. Kono, L. S. I. Veiga, G. Fabbri, D. Haskel, and H. Takagi, Hyperhoneycomb iridate β -Li₂IrO₃ as a platform for Kitaev magnetism, *Phys. Rev. Lett.* **114**, 077202 (2015).
- [2] X. Liu, T. Berlijn, W.-G. Yin, W. Ku, A. Tsvelik, Y.-J. Kim, H. Gretarsson, Y. Singh, P. Gegenwart, and J. P. Hill, Long-range magnetic ordering in Na₂IrO₃, *Phys. Rev. B* **83**, 220403(R) (2011).
- [3] Y. Singh and P. Gegenwart, Antiferromagnetic Mott insulating state in single crystals of the honeycomb lattice material Na₂IrO₃, *Phys. Rev. B* **82**, 064412 (2010).
- [4] J. Chaloupka, G. Jackeli, and G. Khaliullin, Zigzag magnetic order in the iridium oxide Na₂IrO₃, *Phys. Rev. Lett.* **110**, 097204 (2013).
- [5] M. Abramchuk, C. Ozsoy-Keskinbora, J. W. Krizan, K. R. Metz, D. C. Bell, and F. Tafti, Cu₂IrO₃: A new magnetically frustrated honeycomb iridate, *J. Am. Chem. Soc.* **139**, 15371 (2017).
- [6] Y. S. Choi, C. H. Lee, S. Lee, S. Yoon, W.-J. Lee, J. Park, A. Ali, Y. Singh, J.-C. Orain, G. Kim, J.-S. Rhyee, W.-T. Chen, F. Chou, and K.-Y. Choi, Exotic low-energy excitations emergent in the random Kitaev magnet Cu₂IrO₃, *Phys. Rev. Lett.* **122**, 167202 (2019).
- [7] S.-H. Baek, S.-H. Do, K.-Y. Choi, Y. S. Kwon, A. U. B. Wolter, S. Nishimoto, J. van den Brink, and B. Büchner, Evidence for a field-induced quantum spin liquid in α -RuCl₃, *Phys. Rev. Lett.* **119**, 037201 (2017).
- [8] J. Zheng, K. Ran, T. Li, J. Wang, P. Wang, B. Liu, Z.-X. Liu, B. Normand, J. Wen, and W. Yu, Gapless spin excitations in the field-induced quantum spin liquid phase of α -RuCl₃, *Phys. Rev. Lett.* **119**, 227208 (2017).
- [9] Y. Kasahara, K. Sugii, T. Ohnishi, M. Shimozawa, M. Yamashita, N. Kurita, H. Tanaka, J. Nasu, Y. Motome, T. Shibauchi, and Y. Matsuda, Unusual thermal Hall effect in a Kitaev spin liquid candidate α -RuCl₃, *Phys. Rev. Lett.* **120**, 217205 (2018).
- [10] Z. Wang, S. Reschke, D. Hüvonen, S.-H. Do, K.-Y. Choi, M. Gensch, U. Nagel, T. Rößler, and A. Loidl, Magnetic excitations and continuum of a possibly field-induced quantum spin liquid in α -RuCl₃, *Phys. Rev. Lett.* **119**, 227202 (2017).
- [11] G. Jackeli and G. Khaliullin, Mott insulators in the strong spin-orbit coupling limit: From Heisenberg to a quantum compass and Kitaev models, *Phys. Rev. Lett.* **102**, 017205 (2009).
- [12] G. Sala, M. B. Stone, B. K. Rai, A. F. May, D. S. Parker, G. B. Halász, Y. Q. Cheng, G. Ehlers, V. O. Garlea, Q. Zhang, M. D. Lumsden, and A. D. Christianson, Crystal field splitting, local anisotropy, and low-energy excitations in the quantum magnet YbCl₃, *Phys. Rev. B* **100**, 180406(R) (2019).
- [13] J. Xing, E. Feng, Y. Liu, E. Emmanouilidou, C. Hu, J. Liu, D. Graf, A. P. Ramirez, G. Chen, H. Cao, and N. Ni, Néel-type antiferromagnetic order and magnetic field-temperature phase diagram in the spin- $\frac{1}{2}$ rare-earth honeycomb compound YbCl₃, *Phys. Rev. B* **102**, 014427 (2020).
- [14] J. Ji, M. Sun, Y. Cai, Y. Wang, Y. Sun, W. Ren, Z. Zhang, F. Jin, and Q. Zhang, Rare-earth chalcogenides: A family of van der Waals layered Kitaev spin liquid candidates, *Chin. Phys. Lett.* **38**, 047502 (2021).
- [15] Z. Zhang, Y. Cai, J. Kang, Z. Ouyang, Z. Zhang, A. Zhang, J. Ji, F. Jin, and Q. Zhang, Anisotropic exchange coupling and ground state phase diagram of Kitaev compound YbOCl, *Phys. Rev. Res.* **4**, 033006 (2022).
- [16] J. Rodríguez-Carvajal, Recent advances in magnetic structure determination by neutron powder diffraction, *Phys. B (Amsterdam, Neth.)* **192**, 55 (1993).
- [17] J. M. Perez-Mato, S. V. Gallego, E. S. Tasci, L. Elcoro, G. de la Flor, and M. I. Aroyo, Symmetry-based computational tools for magnetic crystallography, *Annu. Rev. Mater. Res.* **45**, 217 (2015).
- [18] M. Fishman, S. R. White, and E. M. Stoudenmire, The ITensor software library for tensor network calculations, *SciPost Phys. Codebases*, **4** (2022).
- [19] M. Fishman, S. R. White, and E. M. Stoudenmire, Codebase release 0.3 for ITensor, *SciPost Phys. Codebases*, **4-r0.3** (2022).
- [20] S. Toth and B. Lake, Linear spin wave theory for single-Q incommensurate magnetic structures, *J. Phys.: Condens. Matter* **27**, 166002 (2015).
- [21] Z.-X. Luo and G. Chen, Honeycomb rare-earth magnets with anisotropic exchange interactions, *SciPost Phys. Core* **3**, 004 (2020).

- [22] Y. Li, G. Chen, W. Tong, L. Pi, J. Liu, Z. Yang, X. Wang, and Q. Zhang, Rare-earth triangular lattice spin liquid: A single-crystal study of YbMgGaO_4 , *Phys. Rev. Lett.* **115**, 167203 (2015).
- [23] P. A. Maksimov, Z. Zhu, S. R. White, and A. L. Chernyshev, Anisotropic-exchange magnets on a triangular lattice: Spin waves, accidental degeneracies, and dual spin liquids, *Phys. Rev. X* **9**, 021017 (2019).
- [24] See Supplemental Material at <http://link.aps.org/supplemental/10.1103/PhysRevResearch.6.033274> for an energy dispersive x ray of $\text{Yb}_x\text{Lu}_{1-x}\text{OCl}$ samples, electron spin resonance spectra of $\text{Yb}_x\text{Lu}_{1-x}\text{OCl}$, the 12-site honeycomb spin lattice size with periodic boundary conditions, AC susceptibility of the magnetic fields in the ab plane and along the c axis of YbOCl , M - H data in the ab plane and along the c axis of YbOCl at 0.5 K, high-temperature range heat capacity of YbOCl , M - H data along the c axis at different temperatures, the Laue diffraction pattern of the YbOCl single crystal, the fitting results of M/H - T and heat capacity, density matrix renormalization group calculation results, the effect of the off-diagonal spin-exchange interactions on M/H - T , and the heat capacity and M/H - T data under different magnetic fields.
- [25] S. Trebst and C. Hickey, Kitaev materials, *Phys. Rep.* **950**, 1 (2022).
- [26] H.-C. Jiang, Z.-C. Gu, X.-L. Qi, and S. Trebst, Possible proximity of the Mott insulating iridate Na_2IrO_3 to a topological phase: Phase diagram of the Heisenberg-Kitaev model in a magnetic field, *Phys. Rev. B* **83**, 245104 (2011).
- [27] Z. Zhu, I. Kimchi, D. N. Sheng, and L. Fu, Robust non-Abelian spin liquid and a possible intermediate phase in the antiferromagnetic Kitaev model with magnetic field, *Phys. Rev. B* **97**, 241110(R) (2018).
- [28] J. A. Sears, L. E. Chern, S. Kim, P. J. Bereciartua, S. Francoual, Y. B. Kim, and Y.-J. Kim, Ferromagnetic Kitaev interaction and the origin of large magnetic anisotropy in α - RuCl_3 , *Nat. Phys.* **16**, 837 (2020).
- [29] A. Banerjee, J. Yan, J. Knolle, C. A. Bridges, M. B. Stone, M. D. Lumsden, D. G. Mandrus, D. A. Tennant, R. Moessner, and S. E. Nagler, Neutron scattering in the proximate quantum spin liquid α - RuCl_3 , *Science* **356**, 1055 (2017).
- [30] C. Kim, J. Jeong, G. Lin, P. Park, T. Masuda, S. Asai, S. Itoh, H. S. Kim, H. Zhou, J. Ma, and J. G. Park, Antiferromagnetic Kitaev interaction in $j_{\text{eff}} = 1/2$ cobalt honeycomb materials $\text{Na}_3\text{Co}_2\text{SbO}_6$ and $\text{Na}_2\text{Co}_2\text{Te}_2\text{O}_6$, *J. Phys.: Condens. Matter* **34**, 045802 (2021).
- [31] H. B. Cao, A. Banerjee, J.-Q. Yan, C. A. Bridges, M. D. Lumsden, D. G. Mandrus, D. A. Tennant, B. C. Chakoumakos, and S. E. Nagler, Low-temperature crystal and magnetic structure of α - RuCl_3 , *Phys. Rev. B* **93**, 134423 (2016).
- [32] F. Ye, S. Chi, H. Cao, B. C. Chakoumakos, J. A. Fernandez-Baca, R. Custelcean, T. F. Qi, O. B. Korneta, and G. Cao, Direct evidence of a zigzag spin-chain structure in the honeycomb lattice: A neutron and x-ray diffraction investigation of single-crystal Na_2IrO_3 , *Phys. Rev. B* **85**, 180403(R) (2012).
- [33] Y. Q. Hao, H. L. Wo, Y. M. Gu, X. W. Zhang, Y. Q. Gu, S. Y. Zheng, Y. Zhao, G. Y. Xu, J. W. Lynn, K. Nakajima, N. Murai, W. B. Wang, and J. Zhao, Field-tuned magnetic structure and phase diagram of the honeycomb magnet YbCl_3 , *Sci. China: Phys., Mech. Astron.* **64**, 237411 (2021).
- [34] A. Banerjee, P. Lampen-Kelley, J. Knolle, C. Balz, A. A. Aczel, B. Winn, Y. Liu, D. Pajerowski, J. Yan, C. A. Bridges, A. T. Savici, B. C. Chakoumakos, M. D. Lumsden, D. A. Tennant, R. Moessner, D. G. Mandrus, and S. E. Nagler, Excitations in the field-induced quantum spin liquid state of α - RuCl_3 , *npj Quantum Mater.* **3**, 8 (2018).
- [35] M. Majumder, M. Schmidt, H. Rosner, A. A. Tsirlin, H. Yasuoka, and M. Baenitz, Anisotropic $\text{Ru}^{3+} 4d^5$ magnetism in the α - RuCl_3 honeycomb system: Susceptibility, specific heat, and zero-field NMR, *Phys. Rev. B* **91**, 180401(R) (2015).
- [36] S. Bachus, D. A. S. Kaib, Y. Tokiwa, A. Jesche, V. Tsurkan, A. Loidl, S. M. Winter, A. A. Tsirlin, R. Valentí, and P. Gegenwart, Thermodynamic perspective on field-induced behavior of α - RuCl_3 , *Phys. Rev. Lett.* **125**, 097203 (2020).
- [37] G. Lin *et al.*, Field-induced quantum spin disordered state in spin-1/2 honeycomb magnet $\text{Na}_2\text{Co}_2\text{TeO}_6$, *Nat. Commun.* **12**, 5559 (2021).
- [38] C. V. Topping and S. J. Blundell, A.C. susceptibility as a probe of low-frequency magnetic dynamics, *J. Phys.: Condens. Matter* **31**, 013001 (2019).
- [39] J. A. Sears, Y. Zhao, Z. Xu, J. W. Lynn, and Y.-J. Kim, Phase diagram of α - RuCl_3 in an in-plane magnetic field, *Phys. Rev. B* **95**, 180411(R) (2017).
- [40] A. U. B. Wolter, L. T. Corredor, L. Janssen, K. Nenkov, S. Schönecker, S.-H. Do, K.-Y. Choi, R. Albrecht, J. Hunger, T. Doert, M. Vojta, and B. Büchner, Field-induced quantum criticality in the Kitaev system α - RuCl_3 , *Phys. Rev. B* **96**, 041405(R) (2017).
- [41] E. Lefrançois, M. Songvilay, J. Robert, G. Nataf, E. Jordan, L. Chaix, C. V. Colin, P. Lejay, A. Hadj-Azzem, R. Ballou, and V. Simonet, Magnetic properties of the honeycomb oxide $\text{Na}_2\text{Co}_2\text{TeO}_6$, *Phys. Rev. B* **94**, 214416 (2016).
- [42] L. Viciu, Q. Huang, E. Morosan, H. W. Zandbergen, N. I. Greenbaum, T. McQueen, and R. J. Cava, Structure and basic magnetic properties of the honeycomb lattice compounds $\text{Na}_2\text{Co}_2\text{TeO}_6$ and $\text{Na}_3\text{Co}_2\text{SbO}_6$, *J. Solid State Chem.* **180**, 1060 (2007).
- [43] A. K. Bera, S. M. Yusuf, A. Kumar, and C. Ritter, Zigzag antiferromagnetic ground state with anisotropic correlation lengths in the quasi-two-dimensional honeycomb lattice compound $\text{Na}_2\text{Co}_2\text{TeO}_6$, *Phys. Rev. B* **95**, 094424 (2017).